



Contents lists available at ScienceDirect

Transportation Research Part C

journal homepage: www.elsevier.com/locate/trc



Evaluation and prediction of transportation resilience under extreme weather events: A diffusion graph convolutional approach[☆]



Hong-Wei Wang^a, Zhong-Ren Peng^b, Dongsheng Wang^a, Yuan Meng^c, Tianlong Wu^c, Weili Sun^{c,*}, Qing-Chang Lu^{d,*}

^a Center for Intelligent Transportation Systems and Unmanned Aerial Systems Applications, State Key Laboratory of Ocean Engineering, School of Naval Architecture, Ocean and Civil Engineering, Shanghai Jiao Tong University, Shanghai 200240, China

^b International Center for Adaptation Planning and Design (iAdapt), School of Landscape Architecture and Planning, College of Design, Construction, and Planning, University of Florida, P.O. Box 115706, Gainesville, FL 32611-5706, USA

^c DiDi Smart Transportation, Haidian District, Beijing 100000, China

^d Future Transportation Research Center, Chang'an University, Xi'an, Shaanxi 710064, China

ARTICLE INFO

Keywords:

Transportation resilience
Extreme weather events
Urban road networks
Spatiotemporal traffic prediction
Graph Convolutional Neural Network
Deep Learning

ABSTRACT

Resilience offers a broad social-technical framework to deal with breakdown, response and recovery of transportation networks adapting to various disruptions. Although current research works model and simulate transportation resilience from different perspectives, the real-world resilience of urban road network is still unclear. In this paper, a novel end to end deep learning framework is proposed to estimate and predict the spatiotemporal patterns of transportation resilience under extreme weather events. Diffusion Graph Convolutional Recurrent Neural Network and a dynamic-capturing algorithm of transportation resilience jointly form the backbone of this framework. The presented framework can capture the spatiotemporal dependencies of urban road network and evaluate transportation resilience based on real-world big data, including on-demand ride services data provided by DiDi Chuxing and grid meteorological data. Results show that aggregate data of related precipitation events could be used for transportation resilience modeling under extreme weather events when facing sample imbalance problem due to limited historical disaster data. In terms of observed transportation resilience, transportation network demonstrates different characteristics between sparse network and dense network, as well as general precipitation events and extreme weather events. The response time is double or triple of the recovery time, and an elastic limit exists in the recovery process of network resilience. In terms of resilience prediction, the proposed model outperforms competitors by incorporating topological information and has better predictions of the system performance degradation than other resilience indices. The above results could assist researchers and policy makers clearly understand the real-world resilience of urban road networks in both theory and practice, and take effective responses under emergent disruptive events.

[☆] This article belongs to the Virtual Special Issue on "Machine learning".

* Corresponding authors.

E-mail addresses: hongweiwang_sjtu@163.com (H.-W. Wang), sunweili@didichuxing.com (W. Sun), qclu@chd.edu.cn (Q.-C. Lu).

1. Introduction

As a concept attracting increasing attention in the transport literature, resilience becomes a new perspective estimating the performance of transportation network and system under disruptions. Transportation resilience can be regarded as the ability of transportation system to withstand and recover from disruptions under extreme conditions, such as public events, terrorist attacks, and natural disasters (Zhu et al., 2017). A major concern for transportation systems of coastal areas is the frequent disasters like hurricane, flooding, and rainstorm. These extreme weather events could cause devastating impacts and even loss of lives, resulting in extensive destruction on the function of transportation infrastructure and system. Thus, if the spatiotemporal distribution patterns of transportation resilience under various extreme weather events can be observed and estimated quantitatively based on traffic performance and disaster data, showing how seriously resilience loses in specific and how long systems can recover in general, the efforts of disaster mitigation and emergency responses could be more effective.

However, different from the substantial literature about impacts of extreme weather on travel activities, capacity, reliability, robustness, and vulnerability of transport system (Lu et al., 2014; Cats and Jenelius, 2015; Chen et al., 2015; Jenelius, 2018), researches on transport system resilience in the post-disaster phases are still rare. Most of existing resilience research utilizes topological methodologies to quantify the resilience of transportation system (Aksu and Ozdamar, 2014; Kepartsoglou et al., 2014; Testa et al., 2015). Generally, the scenarios of resilience are simulated with the successive removal of nodes/links in transport network according to scenarios of disasters, and then measured by the degree or betweenness values after each removal. A common conclusion is that the transport network keeps more resilience with random removal of nodes/links but becomes less resilient when nodes/links are removed under targeted attack strategies. One limitation of these topology-based approaches is that a very realistic description of the behavioral responses to the dynamic effects of a disruption is hard to be captured in an abstract network (Mattsson and Jenelius, 2015). Although topological resilience research can provide significant insights and illustrate the weak points of transport network under extreme weather events, there are still difficulties for general application in a specific transport system when facing the impacts of real-world disasters.

Data-driven transport resilience studies can be treated as attempts to overcome limitations of topology-based studies. In recent years, data-driven approaches (e.g. statistics models and measurement frameworks) and transportation big data (e.g. online car-hailing trajectory data and public transit data) propose new perspectives of reconsidering the transport resilience and covering more types of internal and external threats. The resilience process based on internal threats like traffic accidents and technical failures has been well modelled and estimated by emerging big data technologies (Donovan and Work, 2017; Lu, 2018). However, due to the difficulty of accurately measuring the resilience properties under external threats (e.g. antagonistic attacks, adverse weather conditions, and natural disasters), only a few research attempts to apply data-driven methods to measure transport network resilience under external threats (Loo and Leung, 2017), especially for the case of catastrophic events (Mattsson and Jenelius, 2015). Zhu et al. (2017) explored the spatial recovery patterns of regional subway system resilience in New York City under Hurricane Irene and Hurricane Sandy, which is a recent data-driven attempt for external resilience. However, most of previous studies based on conventional statistical models only provide case studies focusing on certain disaster events, hardly deriving generalized research results and conclusions.

Recently, deep learning exhibits the potentials enhancing the methodology of resilience assessment, and has demonstrated strong performance in general transport researches (Sun and Yin, 2017; Huang et al., 2018), due to its flexible model structure and powerful learning ability (Hao et al., 2019). Recurrent Neural Network series (RNN) methods, such as Long Short-Term Memory Recurrent Network (LSTM) (Ma et al., 2015; Huang et al., 2018), Bidirectional Recurrent Neural Network (BiRNN) (Ma et al., 2018), Sequence to Sequence learning (Seq2Seq) (Sutskever et al., 2014; Liao et al., 2018) and Attention Mechanism (Bahdanau et al., 2014; Wu et al., 2018; Hao et al., 2019; Wang et al., 2020) have shown outstanding performance in capturing long-term temporal dependency and been widely-used in general transport predictions. However, RNN-based models neglect neighboring factors in transport system and is incapable of characterizing spatial correlations. Based on the idea of Convolutional Neural Network (CNN), CNN-LSTM (Wu and Tan, 2016), Conv-LSTM (Ke et al., 2017) and ST-3DNet (Guo et al., 2019) are employed to extract spatiotemporal features and conduct predictions considering Euclidean space in grid-structured data (e.g., images). However, the traffic in transport system contains complex non-Euclidean and directional correlations, which presents stronger topological properties instead of general Euclidean-spatial dependencies. For these graph-structured data, the original CNN is not applicable. To address this problem, Graph Convolutional Neural Network (GCN) is developed to generalize the convolution operator to arbitrary graphs. Generally, GCN can be categorized as spectral approaches and non-spectral approaches. Spectral-based GCN (Bruna et al., 2013) is defined in the Fourier domain by computing the eigendecomposition of the Laplacian matrix and improved by ChebNet (Defferrard et al., 2016) with faster convolution filters. Several attempts have been achieved applying spectral-based GCN to general transport predictions, such as traffic speed in traffic sensor network (Yu et al., 2017; Zhang et al., 2019a, 2019b), station-level demand in bike-sharing network (Lin et al., 2018a) and real-time parking occupancy in parking meter network (Yang et al., 2019). Non-spectral based GCN defines convolutions directly on the graph with operating on groups of spatially close neighbors, such as diffusion convolutional neural network (DCNN) (Atwood and Towsley, 2016), GraphCNN (Hechtlinger et al., 2017) and TGC-LSTM (Cui et al., 2019). Diffusion Graph Convolutional Recurrent Neural Network (DCRNN) (Li et al., 2017) integrates diffusion convolution and the sequence to sequence architecture to model the spatiotemporal dependency of traffic as a diffusion process on directed graph, which is a recently successful attempt to apply Non-spectral based GCN in transport predictions.

In this paper, we aim to propose an end to end deep learning framework to estimate and predict the spatiotemporal patterns of transportation resilience under various extreme weather events. The framework is built based on Diffusion Graph Convolutional Recurrent Neural Network (DCRNN) and a dynamic-capturing algorithm of transportation resilience. The model is designed to simultaneously capture spatiotemporal dependency of transportation resilience from a directed graph. To achieve this goal: (1) The topological information of urban road network is incorporated for spatiotemporal prediction; (2) The spatiotemporal characteristics of urban road resilience are explored quantitatively with real-world big data; (3) Dozens of extreme weather events data are

considered in the model instead of case studies only focusing on certain disasters; (4) The on-demand ride service data in a large-scale urban road network provided by DiDi Chuxing, the largest online car-hailing platform in China, are utilized to support the estimation and prediction of resilience. To the best of our knowledge, this paper is one of the first attempts to apply graph convolutional approaches in modelling transportation resilience of urban road network.

The remainder of the paper is organized as follows. [Section 2](#) introduces DCRNN and the dynamic-capturing algorithm of resilience. [Section 3](#) describes the details of the experiment. [Section 4](#) estimates the characteristics of observed resilience and the prediction performance. A case study on Typhoon Mangkhut is also conducted. Finally, [Section 5](#) concludes this study, illustrates practical implications, and outlooks future research.

2. Methodology

2.1. Preliminaries

Definition 1 (Urban road network topology). A weighted directed graph $G = (V, E, A)$ is defined to represent a urban road network C containing I traffic monitoring sensors, where V is a set of sensor nodes, E is a set of edges and $A \in \mathbb{R}^{I \times I}$ is a weighted adjacency matrix representing the nodes proximity (e.g., pairwise distances between sensors). Denote the time series on G as a graph signal $X \in \mathbb{R}^{I \times N}$, where N is the number of all the features of each node (e.g., traffic flow, meteorological series, etc.).

Definition 2 (Traffic Speed). Tensor $\mathcal{U}_Q \in \mathbb{R}^{I \times N_s}$, $\mathcal{U}_P \in \mathbb{R}^{I \times N_s}$ and $\mathcal{U}_{P'} \in \mathbb{R}^{I \times N_s}$ respectively denote the traffic speed of all the I sensors in next Q hours, past P hours and past $P' = (P + 7 \times 24)$ hours (i.e., last day of week), where N_s is the number of traffic speed features. \mathcal{U}_P and $\mathcal{U}_{P'}$ represent the effects of time of day and day of week in traffic, respectively.

Definition 3 (Meteorological Features). Tensor $\mathcal{V}_P \in \mathbb{R}^{I \times N_e}$ represents the meteorological features of all the I sensors in past P hours, where N_e is the number of meteorological features. The meteorological features include precipitation, temperature, wind speed, wind direction, etc.

Definition 4 (Weather Forecasting Features). Similar to meteorological series, tensor $\mathcal{W}_Q \in \mathbb{R}^{I \times N_w}$ denotes weather forecast features of all the I sensors for next Q hours, where N_w is the number of weather forecast features.

Definition 5 (Key Points of Precipitation). Tensor $R_{day} \in \mathbb{R}^{I \times D \times 24}$ denotes the weather forecast of 24-hour precipitation, where D represents the days in the whole dataset. In R_{day} , we define following key points for each precipitation event: (1) t_0 : the beginning time of the precipitation; (2) t_1 : the time of the peak precipitation; (3) t_2 : the end time of the precipitation. The illustration of these key points can be checked in [Fig. 1](#).

Definition 6 (Key Points of Traffic Speed). Tensor $\mathcal{U}_{day} \in \mathbb{R}^{I \times D \times 24}$ and $\mathcal{F}_{day} \in \mathbb{R}^{I \times D \times 24}$ denote the ground truth and prediction of 24-hour traffic speed. In \mathcal{U}_{day} and \mathcal{F}_{day} , we define following key points in daily traffic speed, based on the corresponding key points of precipitation: (1) m_0 : the speed value at t_0 ; (2) t_0 : the same time equals to t_0 ; (3) m_1 : the lowest speed value between t_0 and t_2 ; (4) t_1 : the time when m_1 is captured; (5) m_2 : within the period $(t_1, t_1 + 3)$, the recovered speed value supposed to be equal to m_0 . If the highest speed value is still less than m_0 , the highest speed is chosen as the value of m_2 ; (6) t_2 : the time when m_2 is captured and confirmed.

Definition 7 (Key Points of Baseline Traffic). The mean hourly traffic speeds in the day of week $\mathcal{U}_{wk} \in \mathbb{R}^{I \times 7 \times 24}$ for all I traffic sensors are utilized as the baseline traffic performance and can be computed as the following steps: (1) find the dates without any precipitation in the dataset; (2) archive traffic data for each sensor in above sunny date; (3) calculate mean hourly speed for Monday, Tuesday, Wednesday, Thursday, Friday, Saturday, and Sunday separately. m_0, m_2 denote speed values at t_0 and t_2 in baseline traffic, respectively.

Problem 1 (Resilience Predictions). The task of resilience prediction is based on results of traffic speed prediction. Thus, the goal of this model is to predict the traffic speed in future for all I traffic monitoring sensors in urban road network. The historical graph signal $X \in \mathbb{R}^{I \times N}$ includes two components: (1) traffic speed \mathcal{U}_P , which is denoted as $X_a \in \mathbb{R}^{I \times N_s}$; (2) auxiliary features $\mathcal{U}_P, \mathcal{V}_P$ and \mathcal{W}_Q , which are denoted as $X_b \in \mathbb{R}^{I \times N_b}$. Note that $N_b = N_s + N_e + N_w$. The predicted graph signal $X_s \in \mathbb{R}^{I \times N_s}$ only contains traffic speed \mathcal{U}_Q . Denote $X^{(t)}$ as the graph signal at time t , the model aims to learn a function h to map P -hour historical graph signals to future Q -hour graph signals, given a graph G :

$$[X^{(t-P+1)}, \dots, X^{(t)}; G] \xrightarrow{h} [X_s^{(t+1)}, \dots, X_s^{(t+Q)}] \quad (1)$$

Based on the 24-hour prediction of traffic speed, we capture the key points on R_{day} , \mathcal{U}_{day} and \mathcal{F}_{day} , and compute the resilience indices.

2.2. Diffusion convolution

The diffusion convolution process is introduced as follows. The basic idea of convolutional neural network (CNN) is to scan across the grid-structured data (e.g., images) with a filter to extract the features. The diffusion convolution develops this idea to solve the general graph-structured modelling issues. Diffusion convolution ([Li et al., 2017](#); [Lin et al., 2018b](#)) is defined as a combination of diffusion processes with random walks on the graph. Specifically, the diffusion step K represents that the maximum K nearest neighbors of each node are convolved by the random walks (with a restart probability $\alpha \in [0, 1]$), as shown in [Fig. 2](#). For each step $i \in \{0, \dots, k\}$, the model searches the neighbors i -step away from a node and computes the transition matrices for this step. The

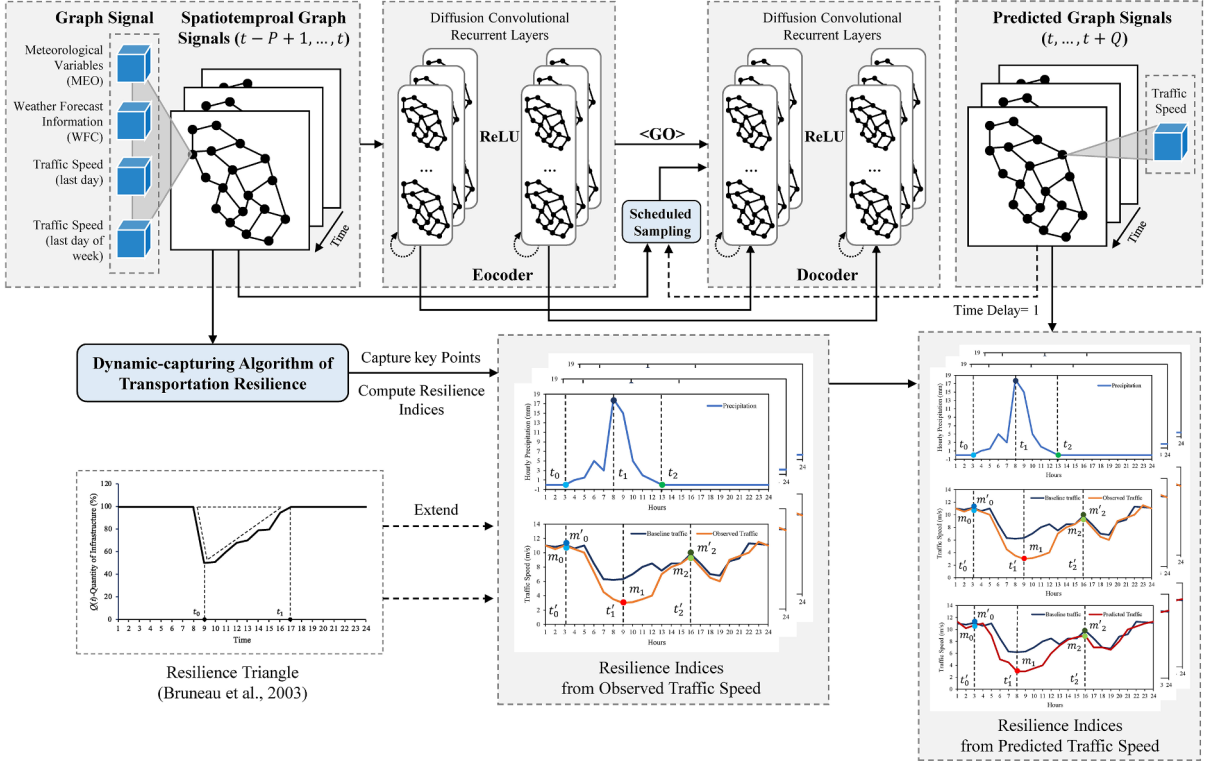


Fig. 1. The end to end deep learning framework based on DCRNN and dynamic-capturing algorithm of transportation resilience.

probability θ , a learnable parameter during model training, is added with the transition matrices to build the diffusion convolutional filter. Thus, the forward diffusion convolution operation $\star F$ over a graph signal $X \in \mathbb{R}^{I \times N}$ and a filter f_θ are defined as:

$$X_{:,n} \star F_\theta = \sum_{k=0}^{K-1} (\theta_k (D^{-1}A)^k) X_{:,n} \quad \text{for } n \in \{0, \dots, N\} \quad (2)$$

where $\theta \in \mathbb{R}^{K \times 1}$ are the parameters for the filter, D represents the out-degree diagonal matrix of the graph and $D^{-1}A$ refers to the transition matrices in diffusion process. If we both consider forward and backward diffusion process to capture the effects from upstream and downstream traffic, the bidirectional diffusion convolution operation $\star B$ is defined as:

$$X_{:,n} \star B_\theta = \sum_{k=0}^{K-1} (\theta_{k,1} (D_{up}^{-1}A)^k + \theta_{k,2} (D_{down}^{-1}A^T)^k) X_{:,n} \quad \text{for } n \in \{0, \dots, N\} \quad (3)$$

where $\theta \in \mathbb{R}^{K \times 2}$ are the parameters for the filter, and $D_{up}^{-1}A$, $D_{down}^{-1}A^T$ represent the transition matrices of forward and backward diffusion process, respectively.

The bidirectional diffusion convolutional layer is defined based on the Eq. (3) with mapping N -dimensional input features to M -dimensional outputs, shown as:

$$H_{:,m} = act \left(\sum_{n=1}^N X_{:,n} \star B_{\theta_{m,n},:} \right) \quad \text{for } m \in \{0, \dots, M\} \quad (4)$$

where $X \in \mathbb{R}^{I \times N}$ is the input, $H \in \mathbb{R}^{I \times M}$ is the output, $\{f_{\theta_{m,n},:}\}$ are the filters and act is the activation function (e.g., ReLU).

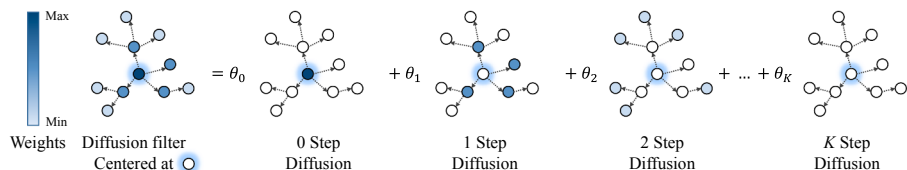


Fig. 2. Illustration of the diffusion process with K diffusion steps on a 3-nearest-neighborhood graph.

2.3. Diffusion graph convolutional sequence to sequence learning

Gated Recurrent Unit (GRU) is powerful variant of Recurrent Neural Network (Cho et al., 2014) to adaptively capture dependencies of different time scales. The initial GRU has two internal gated recurrent units (update gate and reset gate) to capture long-term dependencies. The hidden states $H^{(t)}$ in GRU at time t is calculated by follow:

$$r^{(t)} = \delta(W_{xr}X^{(t)} + W_{hr}H^{(t-1)} + b_r) \quad (5)$$

$$z^{(t)} = \delta(W_{xz}X^{(t)} + W_{hz}H^{(t-1)} + b_z) \quad (6)$$

$$C^{(t)} = \tanh(W_{xc}X^{(t)} + W_{hc}(r^{(t)} \odot H^{(t-1)}) + b_c) \quad (7)$$

$$H^{(t)} = z^{(t)} \odot H^{(t-1)} + (1 - z^{(t)}) \odot C^{(t)} \quad (8)$$

where $r^{(t)}, z^{(t)}$ respectively refer to the state of reset gate and update gate at time t , $C^{(t)}$ and $H^{(t-1)}$ respectively represent reset hidden states at time t and initial hidden states at time $t-1$, $W_{xr}, W_{hr}, W_{xz}, W_{hz}, W_{xc}, W_{hc}$ are the parameters, the variable b_r, b_z, b_c are the bias, the operator \odot refers to the Hadamard product of two matrices, δ and \tanh separately denote logistics sigmoid function and hyperbolic tangent function. We replace the matrix multiplication in GRU with the diffusion convolution to build the Diffusion Convolutional Gated Recurrent Unit (DCGRU).

$$r^{(t)} = \delta(\Theta_r \star B[X^{(t)}, H^{(t-1)}] + b_r) \quad (9)$$

$$z^{(t)} = \delta(\Theta_z \star B[X^{(t)}, H^{(t-1)}] + b_z) \quad (10)$$

$$C^{(t)} = \tanh(\Theta_C \star B[X^{(t)}, (r^{(t)} \odot H^{(t-1)})] + b_c) \quad (11)$$

$$H^{(t)} = z^{(t)} \odot H^{(t-1)} + (1 - z^{(t)}) \odot C^{(t)} \quad (12)$$

where $\star B$ represents the bidirectional diffusion convolution defined in Eq. (3) and $\Theta_r, \Theta_z, \Theta_C$ are learnable parameters for the corresponding filters.

Sequence to Sequence (Seq2Seq) (Cho et al., 2014; Sutskever et al., 2014) is an Encoder-Decoder architecture based on RNN units (e.g. GRU). DCRNN utilizes the Seq2Seq architecture to conduct multi-step predictions, and both encoder and decoder are DCGRU, as shown in Fig. 1. During training process, the input sequences (i.e., all the historical features $X \in \mathbb{R}^{I \times N}$) are fed into encoder and the decoder utilizes the final states of encoder for initialization. Then decoder emits the corresponding results as output sequences given previous ground truth observations. During testing process, the decoder generates predictions, which are compared with ground truth to evaluate the model. Scheduled sampling (Li et al., 2017) is integrated into the model for mitigating the discrepancy between the input distributions in training and testing process. In this way, DCRNN can generate predictions with simultaneously capturing temporal dependency of multi-source inputs and spatial dependency of topological features.

2.4. Dynamic-capturing algorithm of transportation resilience

The Resilience Triangle (Bruneau et al., 2003) is a method to quantify the key features of resilience evaluation: probability of failure, loss of resilience, and duration of recovery, as shown in Fig. 1. In this paper, we extend the idea of Resilience Triangle and propose the resilience indices based on traffic speed fluctuation under extreme weather events, with fully considering the correlation between daily traffic speed and precipitation. Five indices are proposed to quantitatively measure transportation resilience, including Loss of Resilience (LoR), Response Time, Recovery Time, Response Rate, and Recovery Rate. Loss of Resilience refers to the degradation of system performance in urban road network, which is calculated as the difference of values between the enclosed area of baseline traffic performance and the area of the failure triangle in the same day of a week. Response Time represents the period of time between the beginning of extreme events and the time when the worst system performance is caused. Recovery time shows the time period that the system recovers from the worst system performance. Response Rate refers to the speed of system reducing the initial performance to the lowest point of the resilience triangle. Recovery rate demonstrates to the restoration speed of system service.

The above resilience indices are computed according to the key points, which are defined in Definitions 5–7 and shown in Fig. 1. First, we capture the beginning time t_0 , peak time t_1 , and ending time t_2 of a precipitation event within a day. Second, the key points of the speed corresponding to precipitation process are searched and defined, including the beginning point m_0 , the lowest speed point m_1 , and the recovery point m_2 . When the above key points of speed have been captured, the corresponding three time points t_0, t_1, t_2 are also confirmed. Then, the key point m_0, m_2 in baseline traffic are also captured. Thus, resilience indices including Loss of Resilience (LoR), Response Time (RST), Response Rate (RSR), Recovery Time (RCT), and Recovery Rate (RCR) are calculated as:

$$LoR = \int_{t_0}^{t_2} [\mathcal{U}_{wk}(t) - \mathcal{U}_{day}(t)] dt \quad (13)$$

$$RST = t_1 - t_0 \quad (14)$$

$$RSR = \frac{m_0 - m_1}{t_1 - t_0} \quad (15)$$

$$RCT = t_2 - t_1 \quad (16)$$

$$RCR = \frac{m_2 - m_1}{t_2 - t_1} \quad (17)$$

Specifically, the workflow of resilience computation is shown in Algorithm 1. Note that $\mathcal{U}_{day}(t)$ needs to be replaced as $\mathcal{F}_{day}(t)$, when computing resilience indices from traffic speed predictions. The units of proposed resilience indices are listed as follows: (1) The unit of *LoR* is meter (m) and refers to the loss of total travel distance due to external disruptions; (2) The unit of Response Time and Recovery time is hour (h); (3) The unit of Response Rate and Recovery Rate is meter per square second (m/s^2) and refers to the changing rate of traffic speed with respect to time.

Algorithm 1 (Workflow for resilience capturing).

Input The weather forecast of 24-hour precipitation $R_{day} \in \mathbb{R}^{I \times D \times 24}$
 The ground truth of 24-hour traffic speed $\mathcal{U}_{day} \in \mathbb{R}^{I \times D \times 24}$
 The prediction of 24-hour traffic speed $\mathcal{F}_{day} \in \mathbb{R}^{I \times D \times 24}$

Output The ground truth of resilience indices $[LoR, RST, RSR, RCT, RCR]_{ground} \in \mathbb{R}^{N_{res} \times 6}$
 The prediction of resilience indices $[LoR, RST, RSR, RCT, RCR]_{predict} \in \mathbb{R}^{N_{res} \times 6}$

Procedure Resilience Computing
 // Step 1, compute the baseline traffic performance.
 $D_{sun} \leftarrow 0$ // initialize the number of sunny days.
 for d_{th} day in all D days
 for i_{th} sensor in urban road network C
 compute the local daily accumulated precipitation $R_{acc}^{d,i} \in \mathbb{R}^1$ from R_{day}
 end for
 $R_{acc}^d \leftarrow$ the local daily accumulated precipitation of all sensors (\mathbb{R}^I) in d_{th} day
 if R_{acc}^d equals O^I // If the local weathers of all sensors are sunny.
 $D_{sun} += 1$
 $\mathcal{U}_{sun}^{D_{sun}} \leftarrow$ the daily speed of all sensors ($\mathbb{R}^{I \times 24}$) in d_{th} day from \mathcal{U}_{day}
 end for
 // D_{sun} is the number of sunny days in all D days.
 // \mathcal{U}_{sun} is the daily speed ($\mathbb{R}^{I \times D_{sun} \times 24}$) of all sensors in all D_{sun} sunny days.
 for j_{th} day in day of week $J = \{0, 1, 2, 3, 4, 5, 6\}$
 for i_{th} sensor in urban road network C
 compute the mean traffic speed $\mathcal{U}_{wk}^{j,i} \in \mathbb{R}^{24}$ from \mathcal{U}_{sun} corresponding to j_{th} day of week
 end for
 end for
 // \mathcal{U}_{wk} is the mean hourly traffic speeds ($\mathbb{R}^{I \times 7 \times 24}$) in day of week for all sensors and represents the baseline traffic performance in sunny days.

// Step 2, compute resilience indices.
 for i_{th} sensor in urban road network C
 $D_{rain}^i \leftarrow 0$ // initialize the number of rainy dates
 for d_{th} day in all D days
 compute the local daily accumulated precipitation $R_{acc}^{i,d} \in \mathbb{R}^1$ from R_{day}
 if $R_{acc}^{i,d} > 0$
 $D_{rain}^i += 1$
 // The definition of following variables (e.g., $t_0, m_0, etc.$) can be checked in Definition 5, 6, 7.
 search $[t_0, t_1, t_2]$ in $R_{day}^{i,d} \in \mathbb{R}^{24}$ from R_{day}
 search $[m_0, t'_0, m_1, t'_1, m_2, t'_2]_{ground}$ in $\mathcal{U}_{day}^{i,d} \in \mathbb{R}^{24}$ from \mathcal{U}_{day}
 search $[m_0, t'_0, m_1, t'_1, m_2, t'_2]_{predict}$ in $\mathcal{F}_{day}^{i,d} \in \mathbb{R}^{24}$ from \mathcal{F}_{day}
 search $[m'_0, m'_2]$ in $\mathcal{U}_{wk}^{i,d} \in \mathbb{R}^{24}$ in corresponding day of week from \mathcal{U}_{wk}
 // The methods to compute following resilience indices (e.g., LoR, RST, RSR, RCT, RCR , etc.) can be checked in Eq. (13)-(17).
 compute $[LoR, RST, RSR, RCT, RCR]_{ground}^{i,d} \in \mathbb{R}^6$ from the ground truth of 24-hour traffic speed $\mathcal{U}_{day}^{i,d}$
 compute $[LoR, RST, RSR, RCT, RCR]_{predict}^{i,d} \in \mathbb{R}^6$ from the prediction of 24-hour traffic speed $\mathcal{F}_{day}^{i,d}$
 end for
 $D_{rain}^i \leftarrow$ the number of local rainy days in i_{th} sensor
 end for
 $N_{res} \leftarrow$ the number of local rainy days for all sensors $\sum_{k=0}^I D_{rain}^k$
 // The number of local rainy days for sensors in different locations differs.
 output $[LoR, RST, RSR, RCT, RCR]_{ground} \in \mathbb{R}^{N_{res} \times 6}$
 output $[LoR, RST, RSR, RCT, RCR]_{predict} \in \mathbb{R}^{N_{res} \times 6}$
end procedure

3. Data and experiment

3.1. Data description

In this study, Shenzhen, one of the biggest coastal cities in southern China, is selected as the study area, ranging from E113°46' to E114°37' and N22°27' to N22°52'. The traffic datasets are provided by DiDi Chuxing, the largest online car-hailing platform in China,

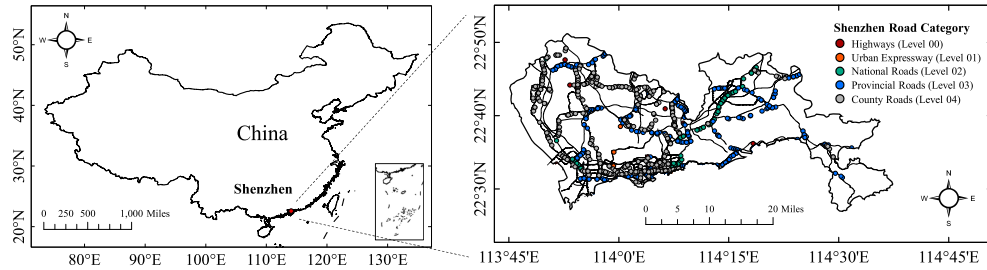


Fig. 3. The location of Shenzhen and the spatial distribution of traffic monitoring sensors.

during the period between Apr. 7, 2017 and Jan. 15, 2019 (totally 649 days). The traffic speed data are computed from DiDi vehicle trajectories (e.g. DiDi Express, DiDi Premier and Tax, roughly accounting for 3–10% of the whole traffic) for each urban road. Virtual pairwise sensors are defined in the geometric centers of the urban roads, with assigning the traffic speed data from upstream and downstream. Totally, there are 1378 virtual sensors, including 34 highways (level 00) sensors, 8 urban expressways (level 01) sensors, 116 national roads (level 02) sensors, 520 provincial roads (level 03) sensors, and 700 county roads (level 04) sensors. Hourly averaged meteorological data in the same period are accessed from the National Center for Atmospheric Research (NCAR), and then processed with the Weather Research and Forecasting (WRF) model to produce grid meteorological and weather forecast data (20×40 points) with a grid spacing of 5 km. Precipitation, temperature, wind speed, wind direction, pressure and humidity are selected as the main meteorological features to reflect the effects of extreme weather events. The traffic-meteorological dataset includes 13 hurricane events (totally covering 30 days, and including 2 red alerts, 2 orange alerts, 6 yellow alerts, 7 blue alerts and 13 white alerts), 63 rainstorm events (including 7 red alerts, 13 orange alerts and 43 yellow alerts), and 207 usual precipitation events. Fig. 3 shows the geographical locations of the sensors.

3.2. Data preprocessing and graph construction

There are several steps for data preprocessing: (1) aggregate all the traffic speed and meteorological readings into 1-hour time intervals and fill missing data with interpolation; (2) find closest meteorological grid for each traffic sensor, then assign meteorological information to this traffic sensor according to the geo-coordinate; (3) form the data to the shape (samples, time steps, sensors, input features) for X and the shape (samples, time steps, sensors, output features) for X_s . In this experiment, the shapes of X and X_s respectively are (642, 24, 1378, 14) and (642, 24, 1378, 1) for 24-hour prediction issues. Note that the number difference (7 days) of samples, compared with the total 649 days in dataset, is caused by building the feature of speed in last day of week; (4) normalize dataset by Z-Score method; (5) 70% of the data are used for training, 20% are used for testing, and the rest 10% for validation.

The topology of the directed road graph is constructed based on the pairwise road network distances between sensors. The weighted adjacency matrix A can be built with threshold Gaussian kernel:

$$A_{ij} = \begin{cases} \exp\left(-\frac{d_{ij}^2}{\sigma^2}\right), & i \neq j \text{ and } \exp\left(-\frac{d_{ij}^2}{\sigma^2}\right) \geq \varepsilon \\ 0, & \text{otherwise.} \end{cases} \quad (18)$$

where A_{ij} refers to the weight of edge, d_{ij} denotes the road network distance between sensor i and j , and σ is the standard deviation of distances. ε is the threshold to control the distribution and sparsity of weight matrix A , assigned to 0.1. The value of ε is determined both considering the experiment results and previous studies (Li et al., 2017; Yu et al., 2017).

3.3. Experiment details and hyper-parameter selections

The experiment is deployed in a Ubuntu 16.04 Linux System with 128 GB RAM and Titan RTX Graphics Cards (24 GB GDDR5 VRAM). Python 3.6 with Pandas, Numpy, Tensorflow, Keras is applied to conduct data processing and modelling. ReLU activation function, Adam optimizer, Mean Square Error (MSE) loss function, and EarlyStoping technique are employed for more effective learning. The hyper-parameters are determined by the performance of the model in validated dataset.

Several statistical indices, including the Symmetric Mean Absolute Percentage Error (SMAPE), the Root Mean Square Error (RMSE), the Mean Absolute Error (MAE) and the Coefficient of Determination (R^2) are employed to evaluate the performance of the proposed model, which are defined as:

$$\text{SMAPE} = \frac{1}{n} \sum_{i=1}^n \frac{|O_i - P_i|}{(|O_i| + |P_i|)/2} \quad (19)$$

$$\text{RMSE} = \sqrt{\frac{1}{n} \sum_{i=1}^n (O_i - P_i)^2} \quad (20)$$

Table 1
Hyper-parameter selection in DCRNN model.

Case	Baseline	Hyperparameter	SMAPE	MAE	RMSE	Running Time/Epoch
Case 1	RNN Units = 256,	Diffusion step = 1	8.6%	0.70	1.08	164.8 s
	RNN Layer = 2,	Diffusion step = 2	8.7%	0.71	1.09	304.7 s
	Horizon = 24	Diffusion step = 3	9.0%	0.73	1.13	429.9 s
Case 2	Diffusion step = 1,	RNN Units = 64	8.9%	0.73	1.16	51.6 s
		RNN Units = 128	8.8%	0.71	1.12	86.9 s
	RNN Layer = 2,	RNN Units = 256	8.6%	0.70	1.08	164.8 s
Case 3	Horizon = 24	RNN Units = 512	8.7%	0.71	1.09	334.4 s
	RNN Units = 256,	RNN Layer = 1	8.8%	0.72	1.09	59.7 s
	Diffusion step = 1,	RNN Layer = 2	8.6%	0.70	1.08	164.8 s
	Horizon = 24	RNN Layer = 3	8.6%	0.69	1.08	304.3 s

$$\text{MAE} = \frac{1}{n} \sum_{i=1}^n |O_i - P_i| \quad (21)$$

$$R^2 = 1 - \frac{\sum_{i=1}^n (O_i - P_i)^2}{\sum_{i=1}^n (O_i - \bar{O}_i)^2} \quad (22)$$

where O_i refers to the observations (ground truth), P_i denotes the predictions, n represents the number of samples, and \bar{O}_i is the mean of O_i .

Table 1 summarizes the effects of three key hyper-parameters: diffusion steps of the graph convolutional filter, number of hidden units in each layer, and layers in the model. Diffusion step roughly corresponds to the size of filters' reception field. The model can capture broader spatial dependency with larger size of reception field, but the learning complexity also grows. In Case 1, with the diffusion steps increasing from 1 to 3, RMSE of predictions presents a light drop from 1.08 to 1.13 and the time cost of computing notably increases from 164.8 s to 429.9 s. The results demonstrate that the accuracy of speed predictions exhibits more dependency on neighboring roads instead of farther spatial-correlated roads, which is lightly different from the application results of DCRNN model in the highway network (Li et al., 2017). The phenomenon is probably caused by the higher intensity of urban road network and more frequent change of urban traffic speed. The number of hidden units and layers represent width and depth of the network, which are the direct representations of the learning capacity of a neural network. In Case 2, the accuracy of speed predictions increases and then keeps roughly stable, when the hidden units grow from 64 to 512. Meanwhile, the time cost rises continuously with the increase of hidden units. In Case 3, similar behaviors are observed for varying the number of layers. Thus, finally {1, 256, 2} are chosen for the values of above three hyper-parameters both considering accuracy of predictions and time cost.

4. Results and discussion

4.1. Evaluation of observed transportation resilience

In Fig. 4(a) and (b), LoR under general precipitation events (including hurricane events, rainstorm events and usual precipitation events) has similar resilience performance on different levels of road, but presents more loss with increase of precipitation. This result demonstrates that degree of failure of urban road network is more decisive by levels of external disruptions instead of their own spatial and temporal features. Generally, the response time is double or triple of the recovery time. The response time of higher level roads like highway (level 00) is longer than that of lower level roads like county roads (level 04). When precipitation becomes heavier, Response time presents generally increase. Compared with response time, recovery time is more stable for different levels of road and intensities of precipitation. These results indicate that response time is more sensitive to environmental changes but recovery time turns out to be more robust. The response rate and recovery rate suggest a relatively equal balance at all scenarios and a slightly increase with the increase of precipitation. Results demonstrate that the degradation of system performance during response period is also double or triple of that of recovery activities.

During extreme weather events, as shown in Fig. 4(c) and (d), LoR and response time present an obvious growth when the alert levels of hurricane and rainstorm are upgraded, compared with the indices in general precipitation days. However, recovery time, response rate, and recovery rate are relatively stable when these disruption events occur. Results illustrate that the characteristics of urban transportation resilience under catastrophic events present similar patterns to those of general precipitation events but are more sensitive. This finding provides a solid foundation of applying general precipitation events data to model the transportation resilience under extreme weather events, when facing the sample imbalance problem due to limited historical disaster data.

In terms of spatial characteristics of urban road resilience, as shown in Fig. 5, LoR is notably larger in the middle west, middle east, and southeast of Shenzhen, where the local road networks are relatively sparse. Considering results in Fig. 4(a), the spatial

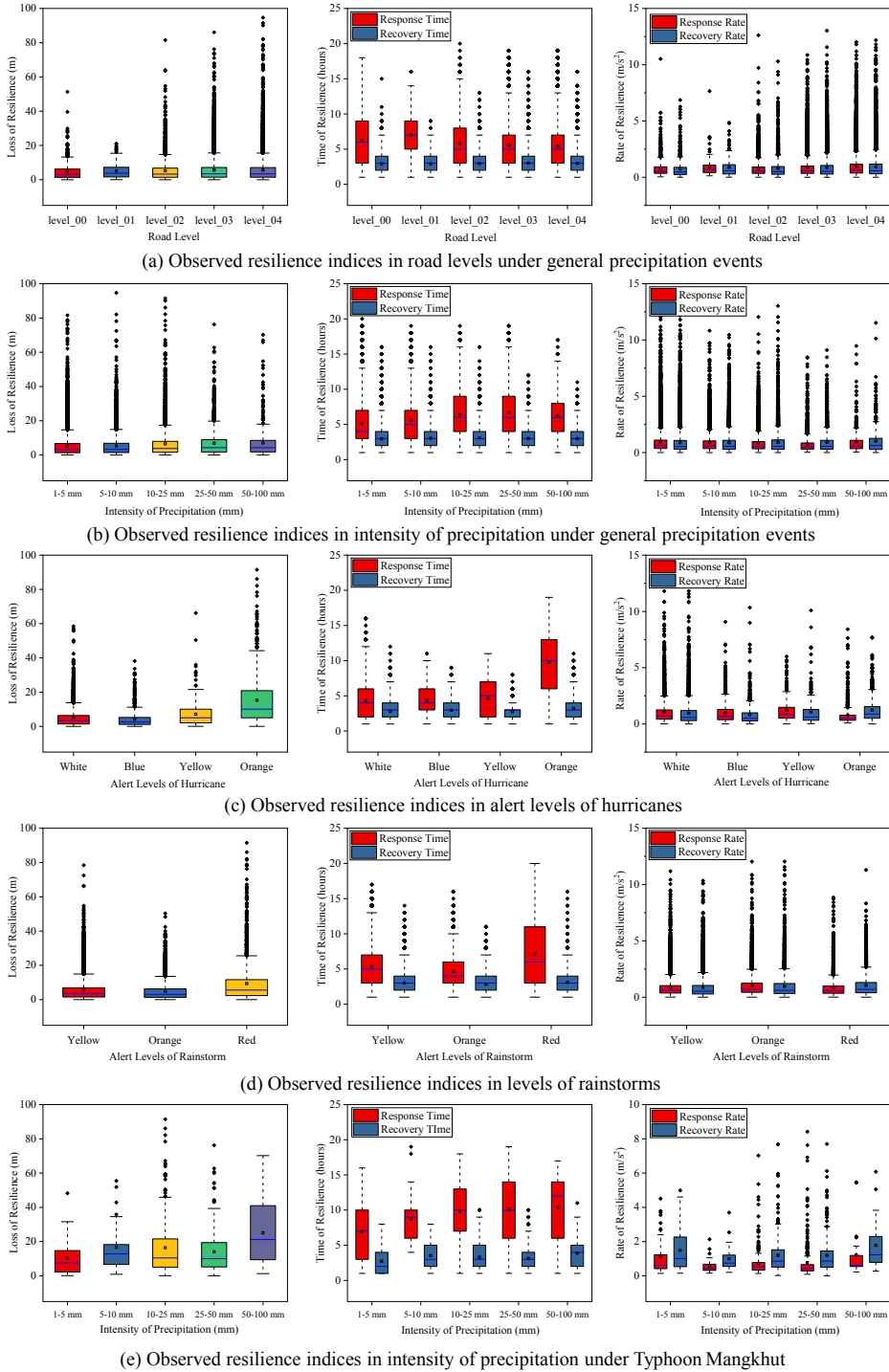


Fig. 4. Characteristics of observed resilience.

distribution of *LoR* is more associated with network intensity instead of road levels. Moreover, the spatial distribution of response rate is almost inverse to that of *LoR*. Areas with larger *LoR* present slower response process. In the areas with less loss of resilience and shorter response time like western, southern, and eastern Shenzhen, the response rate is higher. The results demonstrate that roads with serious ability failures are commonly not the ones having rapid degradation. The local sparse networks with small ability failure are more vulnerable. Recovery rate presents a spatial distribution pattern similar to *LoR*, which means that the serious failures

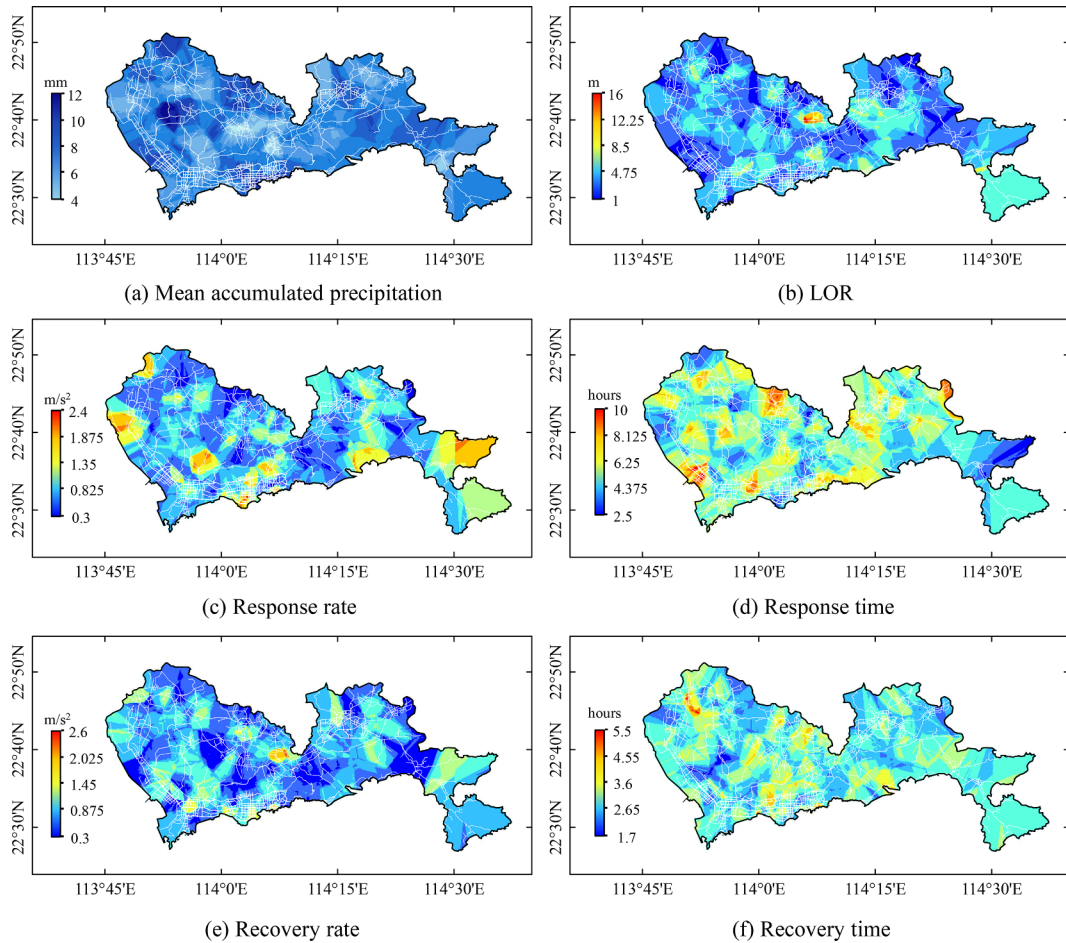


Fig. 5. Spatial characteristics of observed resilience under general precipitation events.

recover quickly but small failures restore slowly. These results indicate that urban road system has a strongly elastic property instead of plasticity.

4.2. Prediction performance of traffic speed

4.2.1. Comparison of models

In this study, the key points of resilience indices are captured from traffic speed. Thus, the accuracy of spatiotemporal prediction in traffic speed is decisive for the computation of the following resilience indices. In this section, a comparison of 6-hour, 12-hour, and 24-hour traffic prediction is conducted. Several widely-used deep learning models are employed to compare with DCRNN. All the baseline models are trained, validated, and tested with roughly the same parameters of DCRNN, and briefly introduced as follows:

- (1) LSTM: Long Short-Term Memory network (Hochreiter and Schmidhuber, 1997; Ma et al., 2015) is a recurrent neural network with multiplicative units (input, output and forget gates). LSTM can well capture long-term temporal dependency and has been widely applied in general transport predictions.
- (2) GRU: Gated recurrent unit (Cho et al., 2014; Fu et al., 2016) is another variant of recurrent neural networks. Similar to LSTM, GRU has internal gated recurrent units (update gate and reset gate) to capture long-term dependencies.
- (3) Bi-LSTM: Bidirectional Recurrent Neural Networks (BiRNN) (Schuster and Paliwal, 1997) can get information from past and future states. Combining BiRNN with LSTM derives Bidirectional LSTM (Bi-LSTM) (Ma et al., 2018), which exhibits a superior ability to model long-range time series in both input directions.
- (4) Bi-GRU: Combining BiRNN with GRU derives Bidirectional GRU (Bi-GRU) (Wang et al., 2017).
- (5) Seq2Seq: Sequence to Sequence model (Sutskever et al., 2014; Liao et al., 2018) is an encoder-decoder architecture based on RNN units and can well address issues of temporal modelling.
- (6) S2S-Att: Attention-based Seq2Seq (Bahdanau et al., 2014; Wu et al., 2018; Hao et al., 2019; Wang et al., 2020) is an encoder-decoder architecture with attention mechanism and can capture dynamic temporal dependency between source sequences and

Table 2

Model comparison between DCRNN and the baseline models.

Models	6-h			12-h			24-h		
	SMAPE	MAE	RMSE	SMAPE	MAE	RMSE	SMAPE	MAE	RMSE
DCRNN	7.2%	0.67	1.03	8.1%	0.68	1.07	8.6%	0.70	1.08
GCRNN	7.3%	0.70	1.07	8.3%	0.72	1.12	8.9%	0.73	1.13
S2S-Att	8.3%	0.81	1.13	9.2%	0.86	1.21	9.9%	0.88	1.26
Seq2Seq	8.4%	0.82	1.15	9.9%	0.88	1.27	11.0%	0.91	1.31
Bi-LSTM	8.8%	0.85	1.17	10.3%	0.92	1.29	11.4%	0.94	1.33
Bi-GRU	8.9%	0.86	1.18	10.3%	0.92	1.30	11.5%	0.95	1.34
LSTM	9.1%	0.89	1.21	10.7%	0.97	1.35	11.7%	0.98	1.37
GRU	9.2%	0.90	1.22	10.8%	0.97	1.36	11.8%	0.99	1.38

target sequences.

The results of model comparison are concluded in [Table 2](#): (1) In RNN-based methods, bidirectional RNNs (i.e., Bi-LSTM and Bi-GRU) exhibit stronger prediction performances for all forecasting horizons, compared with LSTM and GRU; (2) Between encoder-decoder methods and RNN-based methods, Seq2Seq outperforms bidirectional RNNs. Results demonstrate that the encoder-decoder architecture is more adept at handling high-dimension data and nonlinear mapping issues; (3) In encoder-decoder methods, the S2S-Att exceeds Seq2Seq, especially in the case of 24-hour forecasting. Result indicates that the attention mechanism is effective in improving long-term prediction; (4) DCRNN presents a notable increase of prediction precision compared with the temporal encoder-decoder methods (i.e., S2S-Att) and achieves the best performance for all the metrics and forecasting horizons. Result demonstrates that DCRNN can effectively capture the spatiotemporal dependency incorporating topological features. Given that the historical average model (HA), the autoregressive integrated moving average model (ARMA), the support vector regression (SVR), the feed-forward neural network (FNN), the time delay neural network (TDNN), and Kalman filter (KF) have been proven to reach poorer performances than LSTM ([Ma et al., 2015](#); [Huang et al., 2018](#); [Lin et al., 2018a](#); [Zhang et al., 2019a, 2019b](#)) and GRU ([Fu et al., 2016](#)) in recent research on general transport predictions, these statistical time-series models or machine learning models are not listed in this comparison.

[Fig. 6](#) presents quantitative comparisons of models from perspectives of time series and scatters. Considering Typhoon Mangkhut landed on Shenzhen on Sep. 16, 2018 and brought heavy precipitation around this date, we selected a time period between Sep. 11, 2018 and Sep. 20, 2018 to evaluate the temporal prediction performance of these models under the extreme weather events, as shown in the time series. The scatter plots present the observed and predicted traffic speed in the test dataset for overall evaluation of predictions. As shown in [Fig. 6\(a\)](#), (c) and (d), in the period before the typhoon landing (Sep. 11–15), DCRNN, S2S-Att and Seq2Seq can well catch the fluctuates of traffic speed and DCRNN exhibits light superiority when traffic starts to be affected by the arriving typhoon in Sep. 15. In the period of the typhoon landing and passing (Sep. 16–17), DCRNN can almost precisely catch the abnormal fluctuations of traffic speed, however, S2S-Att and Seq2Seq present much more errors when traffic speed influenced by the typhoon. In the period after the typhoon (Sep. 18–20), the minimum value of daily traffic speed is significantly lower than that of the period before the typhoon landing. DCRNN presents notable advantages in capturing this new temporal pattern of traffic speed, however, S2S-Att and Seq2Seq almost suggest similar predictions as usual. In the comparison among DCRNN and other baseline models (e.g., Bi-LSTM, Bi-GRU), similar behaviors are observed in [Fig. 6\(e\)–\(h\)](#). The results illustrate that DCRNN notably outperforms all the baseline models in capturing the special fluctuate of traffic speed under extreme weather events. The R^2 values between predictions and observations demonstrates that 95%, 89%, and 87% of the explained variance are captured by DCRNN, S2S-Att and Seq2Seq. For other baseline models, the R^2 values are even lower (84–86%). The scatter plots demonstrate that predictions of DCRNN are more consistent with the observations in the test dataset. In summary, DCRNN presents distinct advantages in capturing spatiotemporal dependencies of traffic speed under precipitation events and is competent to be employed in resilience predictions.

4.2.2. Impact of graph construction

In order to evaluate the effect of graph construction, an undirected graph is constructed by setting $\hat{A}_{ij} = \hat{A}_{ji} = \max(A_{ij}, A_{ji})$, where \hat{A} is a symmetric matrix generated from A . Based on the undirected graph, GCRNN is developed as a variant of DCRNN with roughly the same architecture and parameters. [Table 2](#) summaries the comparison results of DCRNN and GCRNN. DCRNN outperforms GCRNN in both long-term and short-term predictions. However, GCRNN still suggests significant superiority than S2S-Att and Seq2Seq in all the horizons. In [Fig. 6\(b\)](#), GCRNN presents reliable prediction ability in the period before the typhoon landing (Sep. 11–15) and after the typhoon passing (Sep. 18–20), but still cannot well catch the abnormal fluctuate of traffic speed when the typhoon landing and passing (Sep. 16–17). The R^2 value (93%) of GCRNN indicates that the predictions are more consistent with observations than the baseline models, but still cannot catch up with DCRNN. In summary, GCRNN can outperform baseline temporal models with capturing spatiotemporal dependency. However, DCRNN can achieve better predictions under extreme weather events, with integrating asymmetric properties of urban road network in the directed graph.

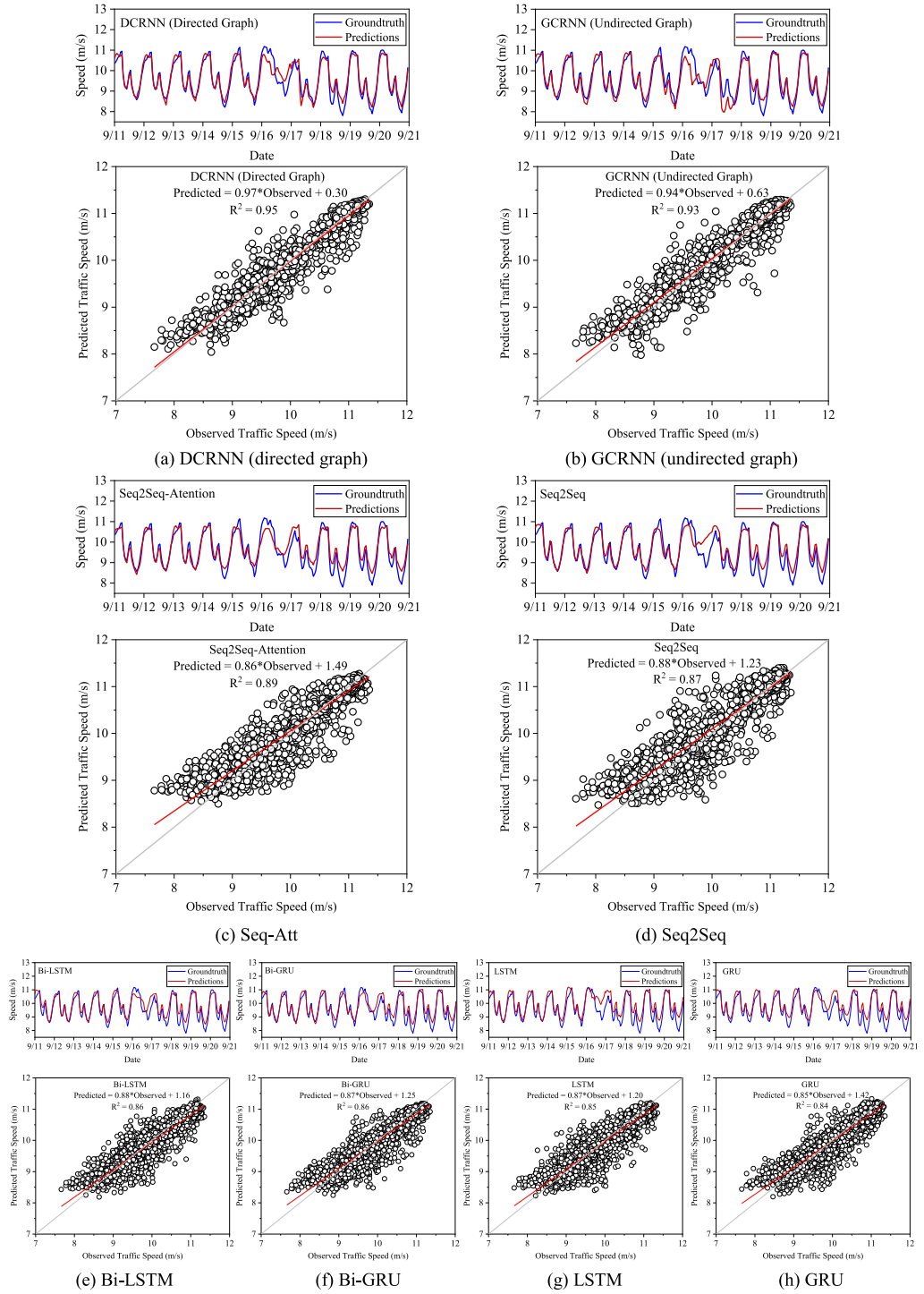


Fig. 6. Time series and scatters of observed and predicted speed in DCRNN and baseline models.

Table 3

Effect of input features in traffic speed predictions.

Case	Input variable groups	Features	SMAPE	MAE	RMSE
Case 1	Speed (last day) + Speed (last day of week) + MEO + WFC	14	8.6%	0.70	1.08
Case 2	Speed (last day) + MEO + WFC	13	9.1%	0.73	1.13
Case 3	Speed (last day) + MEO	7	9.2%	0.75	1.14
Case 4	Speed (last day) + Speed (last day of week)	2	9.1%	0.74	1.14
Case 5	Speed (last day)	1	9.4%	0.76	1.16

4.2.3. Impact of external features

Table 3 indicates the impacts of external traffic, meteorological and weather forecasting features. We remove external variables one by one and measure the change of prediction accuracy under a 24-hour prediction case. The predictive performance decreases significantly (Case 2) when eliminating the historical effect of day of week. The predictive performances exhibit continuous drop (Case 3 and 5) when the meteorological variable group (MEO) and weather forecast variable (WFC) are removed. If we only use the combination (Case 4) of speed in last day and speed in last day of week, the prediction performance roughly corresponds to the results in Case 2. The worst prediction (Case 5) is achieved with only inputting speed in last day. These results indicate that the speed in last day of week and general meteorological information can both independently improve model performance. Considering all these external features can even further enhance the prediction precision.

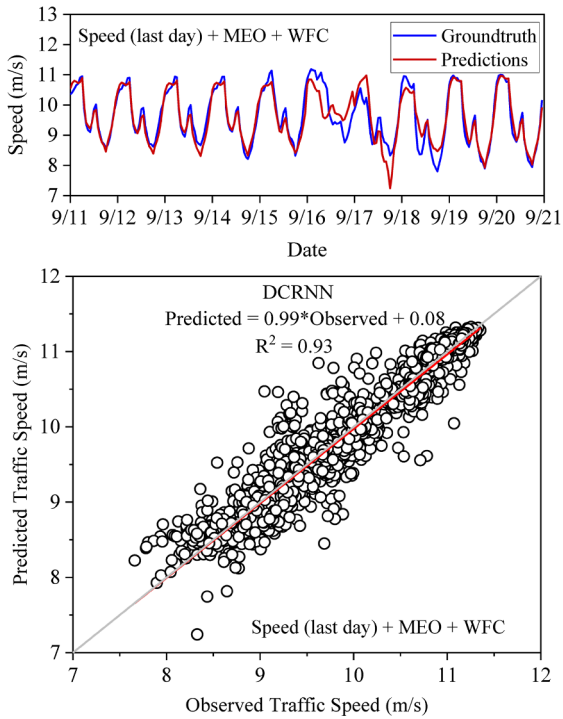
Fig. 7 presents a possible explanation of the above phenomena. When only considering meteorological information and speed in last day, DCRNN can well reflect the effect of Typhoon Mangkhut in Sep. 16–17, as shown in **Fig. 7(a)** and **(b)**. However, the model tends to strengthen the influence of extreme weather events on traffic and underestimate the traffic speed after the typhoon passing (Sep. 18). Compared with **Fig. 6(a)**, the R^2 values (93% and 92%) are also lower than that of considering all the external features (95%). When only considering the historical speed in last day and last day of week, DCRNN exhibits powerful ability to model diurnal variation of speed and difference between weekday and weekend, as shown in **Fig. 7(c)**. However, the model just predicts the traffic speed on Sep. 15–16 as usual and cannot infer any predictions containing the influence of Typhoon Mangkhut. This phenomenon is even more serious in **Fig. 7(d)**, with only considering the speed in last day. The R^2 value also shows a similar decrease from 92% to 91%. These results illustrate that the meteorological information brings DCRNN the ability to consider effects of extreme weather events but causes stronger fluctuation in predictions. The historical speed brings DCRNN more periodicity and alleviates the abnormal fluctuation in predictions. This is the reason why integrating all external features can enhance resilience predictions.

Considering that the extreme weather does not occur often, the limited size of the samples under the extreme weather events probably leads to a potential sample imbalance problem when training the proposed model. There are some efforts to conquer the issue: (1) As shown in **Fig. 4** and discussed in **Section 4.1**, the characteristics of urban transportation resilience under catastrophic events have generally similar patterns to those under general precipitation events. Thus, we incorporated the rainstorm and usual precipitation events data into data set to strengthen the model training. (2) Generally, the aggregate data set (totally 649 days) contain 300 general precipitation events (30 hurricanes days, 63 rainstorm days and 207 usual precipitation days). Therefore, 46.22% of data in the data set is related to general precipitation events, which alleviates the sample imbalance problem. (3) As discussed in **Sections 4.2.1–4.2.3**, the model presents excellent prediction performance, which confirms the aggregate data is effective. Moreover, the adoption of DCRNN, directed graph and external features is verified to strongly improve the ability of modeling the abnormal fluctuation of traffic speed caused by the extreme weather events. In sum, the aggregate data and the methods of modelling work together to conquer the above issue and strengthen the model ability of capturing the effect of extreme weather events.

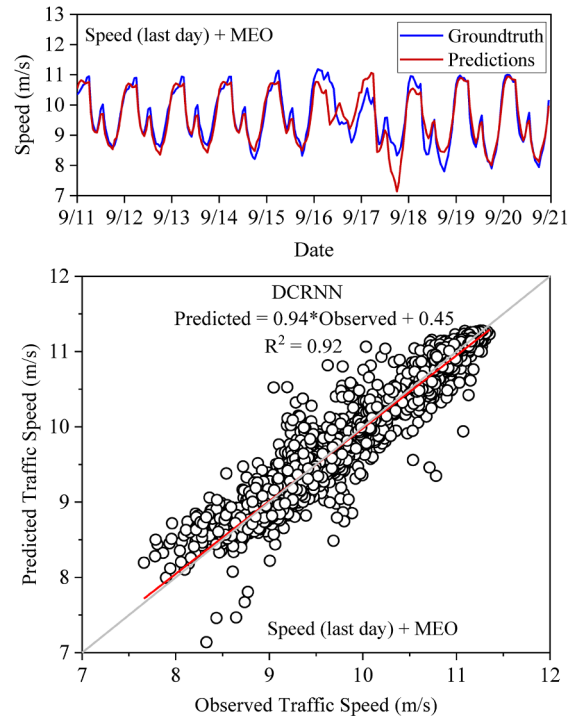
4.3. Characteristics of traffic and resilience predictions

Fig. 8(a)–(d) present the characteristics of predicted speed and resilience indices. In **Fig. 8(a)** and **(c)**, the RMSE of speed of highway (level 00) and expressway (level 01) is quite higher than that of other urban roads (levels 02–04). Meanwhile, similar characteristics are observed for the RMSE of LOR, response rate and recovery rate. These results demonstrate that DCRNN predictions on urban roads outperform those on highways, and the accuracy of traffic predictions strongly affects the accuracy of resilience predictions. In **Fig. 8(b)** and **(d)**, RMSE of speed presents a general increase under 1–70 mm precipitation and a fluctuant rise when the precipitation goes over 70 mm. RMSE of resilience indices even present a more obvious rise with the increase of accumulated precipitation. The result indicates that heavy precipitation can notably decrease the prediction performance, but the proposed model can maintain a stable performance during light and medium precipitation periods. In all categories of roads and intensities of precipitation, RMSE of response rate is lower than that of recovery rate. This result indicates that the proposed model is more adept at handling the prediction of the response process rather than the restoration activities.

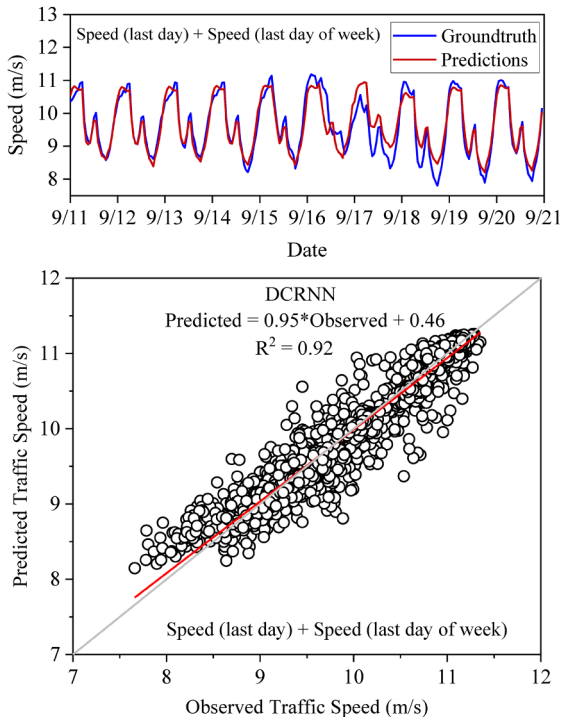
The spatial characteristics of speed prediction and resilience prediction are shown in **Fig. 9** and **Fig. 10**. In **Fig. 9(a)–(c)**, the statistical indices of speed prediction are higher in eastern areas and lower in northwestern Shenzhen. RMSE of LoR in southeastern Shenzhen is notably higher than other areas in **Fig. 10(a)**, which is almost consistent with the spatial characteristics of speed prediction. Compared with **Fig. 10(b)** and **Fig. 5(c)**, the RMSE distribution of predicted response rate is almost inverse to the distribution



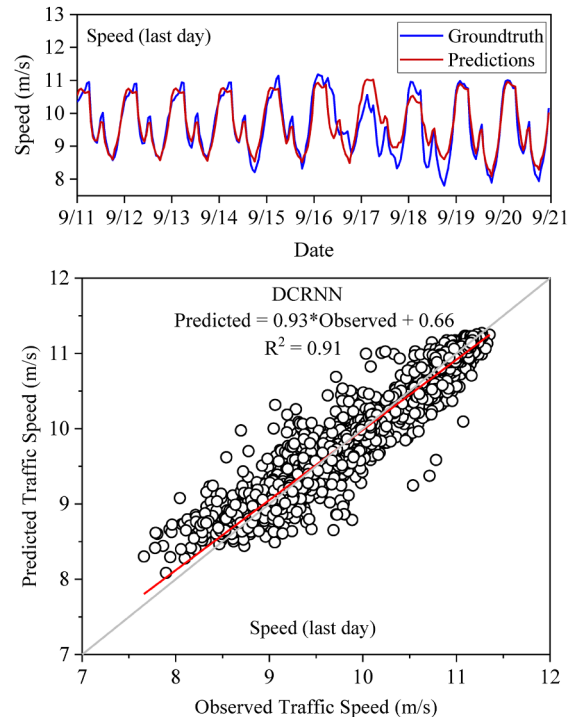
(a) Speed (last day), MEO and WFC



(b) Speed (last day) and MEO



(c) Speed (last day) and Speed (last day of week)



(d) Speed (last day)

Fig. 7. Time series and scatters of observed and predicted speed in DCRNN with integrating different external features.

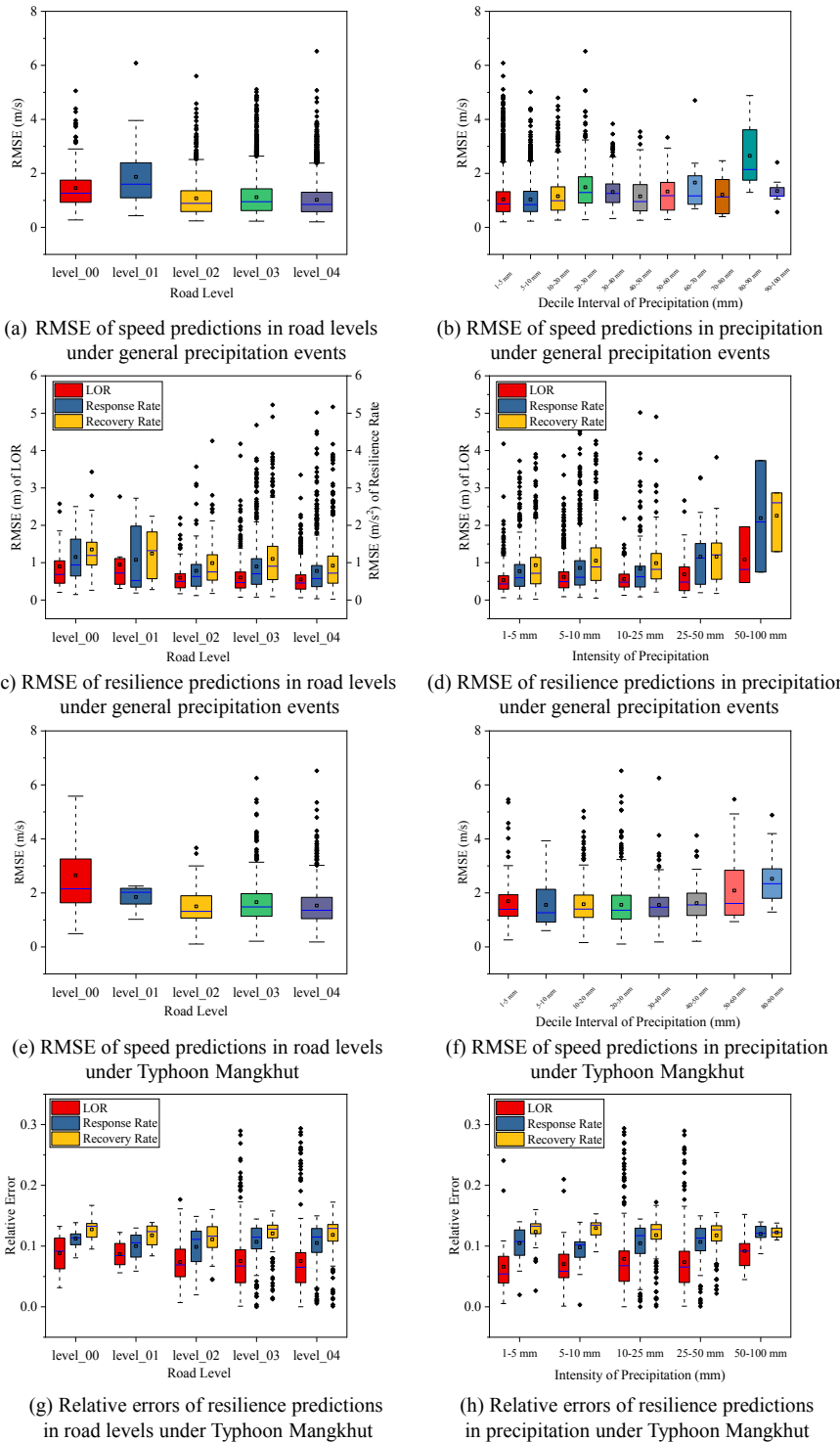


Fig. 8. Statistics indices of speed and resilience predictions in the proposed framework.

pattern of observed response rate, such as the eastern bay area, northwest area, and northeast area. In Fig. 10(c) and Fig. 5(e), similar findings could be reached for the distribution of observed recovery rate and RMSE of recovery rate predictions. These results illustrate that the roads both with quick response and rapid recovery process suggest better prediction accuracy and vice versa. The proposed model is more adept at conducting resilience predictions in roads with strong responses to disruptions.

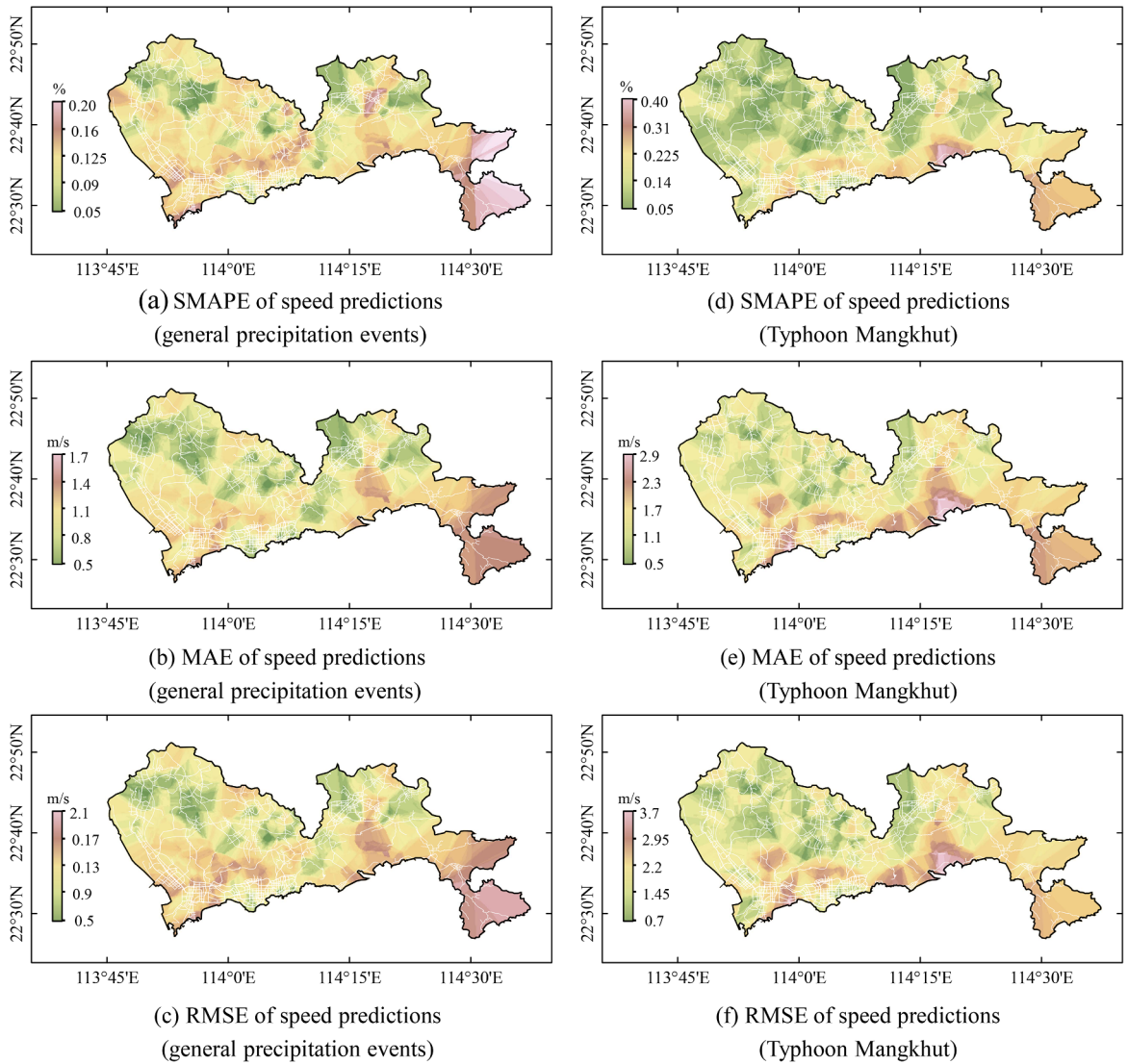


Fig. 9. Spatial distribution of statistics indices in speed predictions.

4.4. Case study on Typhoon Mangkhut

4.4.1. Estimation of observed resilience under Typhoon Mangkhut

Typhoon Mangkhut is a Super Typhoon (the strongest typhoon in the Grade of Tropical Cyclones, China) which caused devastating disruptions in Southern China in 2018. It is the strongest typhoon affecting Shenzhen since 1983. The characteristics of observed resilience under Typhoon Mangkhut are estimated under different precipitation intensity, as shown in Fig. 4(e). *LoR* presents a fluctuant increase when the intensity of precipitation increases, and a sudden rise when local accumulated precipitation exceeds 50 mm. Compared with the relatively balanced *LoR* in general precipitation days in Fig. 4(b), *LoR* under Typhoon Mangkhut is much higher and more sensitive to precipitation. This result illustrates that the hurricane can bring more serious failures than general precipitation events even with the same precipitation intensity. The response time achieves a notable growth when precipitation increases, which is double or triple of the recovery time. There are similar variation trends between response time and recovery time in general precipitation days in Fig. 4(b). However, the response time under Typhoon Mangkhut is at least double of that in general precipitation days. The result indicates that the response time is more sensitive to the degree of disruptions than recovery time. Under Typhoon Mangkhut, the recovery rate is almost double of the response rate, however, the recovery rate is roughly equal to the response rate in general precipitation days. These phenomenon demonstrates that *LoR* during response period is almost the same as that of recovery activities under Typhoon Mangkhut.

The spatial patterns of resilience indices in Typhoon Mangkhut are shown in Fig. 11. *LoR* is larger in the middle and east of Shenzhen in Fig. 11(b), which presents a similar distribution pattern to that of general precipitation days in Fig. 5(b). Except for the

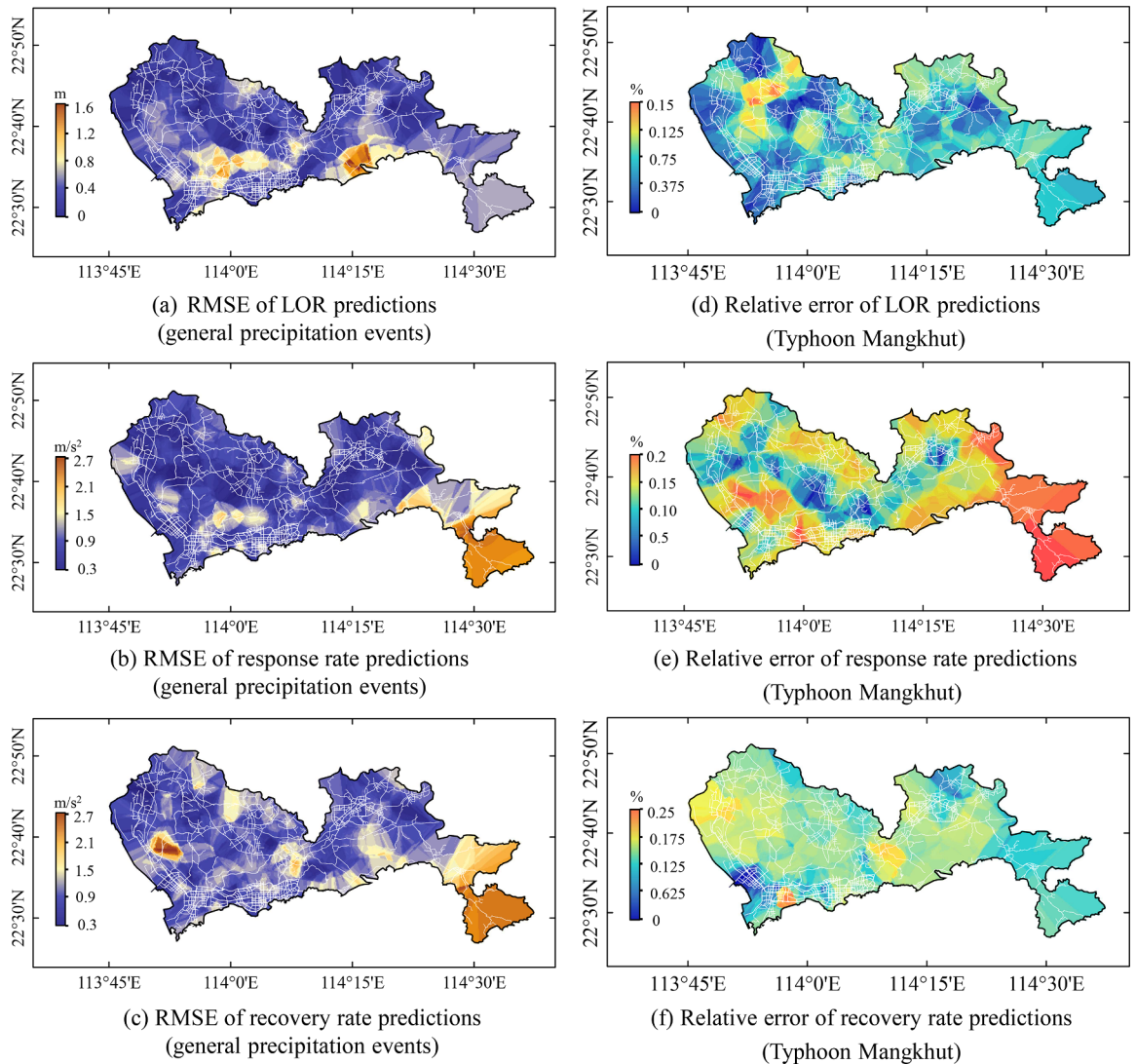


Fig. 10. Spatial distribution of statistics indices in resilience predictions.

northeastern area, response rate and recovery rate suggest nearly inverse distributions to that of LoR, as shown in Fig. 11(c) and (e). These findings demonstrate that the roads with severe failure are commonly not the roads facing quick degradation, which is consistent with the conclusion of response rate in general precipitation days (Fig. 5(c)). In terms of recovery rate, the roads with larger LoR present slower restore activities during Typhoon Mangkhut. However, serious failures could recover quickly in general precipitation days (Fig. 5(e)), which is contrary to what found during Typhoon Mangkhut. This illustrates that an elastic limit probably exists in the process of resilience. Elastic limit originally is a concept in material science and refers to the maximum extent to which a solid may be stretched without permanent alteration of size or shape. Under general precipitation events, the disruption of the transportation system is relatively limited, and the system presents more elasticity. Serious impacts cause rapid restoration, just like harder force results in quicker rebound. However, under hurricane events, the destructions on urban road network are so serious that exceed the limit. Thus, the system demonstrates more plasticity. Severe disruptions cause slower recovery and permanent damages.

4.4.2. Performance of predictions under Typhoon Mangkhut

The characteristics of speed and resilience predictions under Typhoon Mangkhut are estimated by levels of road and intensities of precipitation, as shown in Fig. 8(e)–(h). In Fig. 8(e), RMSEs of speed predictions on highways and expressways are still higher than that of urban roads. This result is generally consistent with the characteristics of speed predictions in general precipitation events (Fig. 8(a)). In Fig. 8(f), the accuracy of speed prediction keeps stable and then presents a sudden rise when precipitation grows over 50 mm, which is more sensitive to the effect of precipitation compared with the characteristics of speed prediction in general precipitation events (Fig. 8(b)). Overall, RMSE of speed prediction under Typhoon Mangkhut is higher than that of general precipitation events, but exhibits similar characteristics for different levels of road and intensities of precipitation. In Fig. 8(g) and (h),

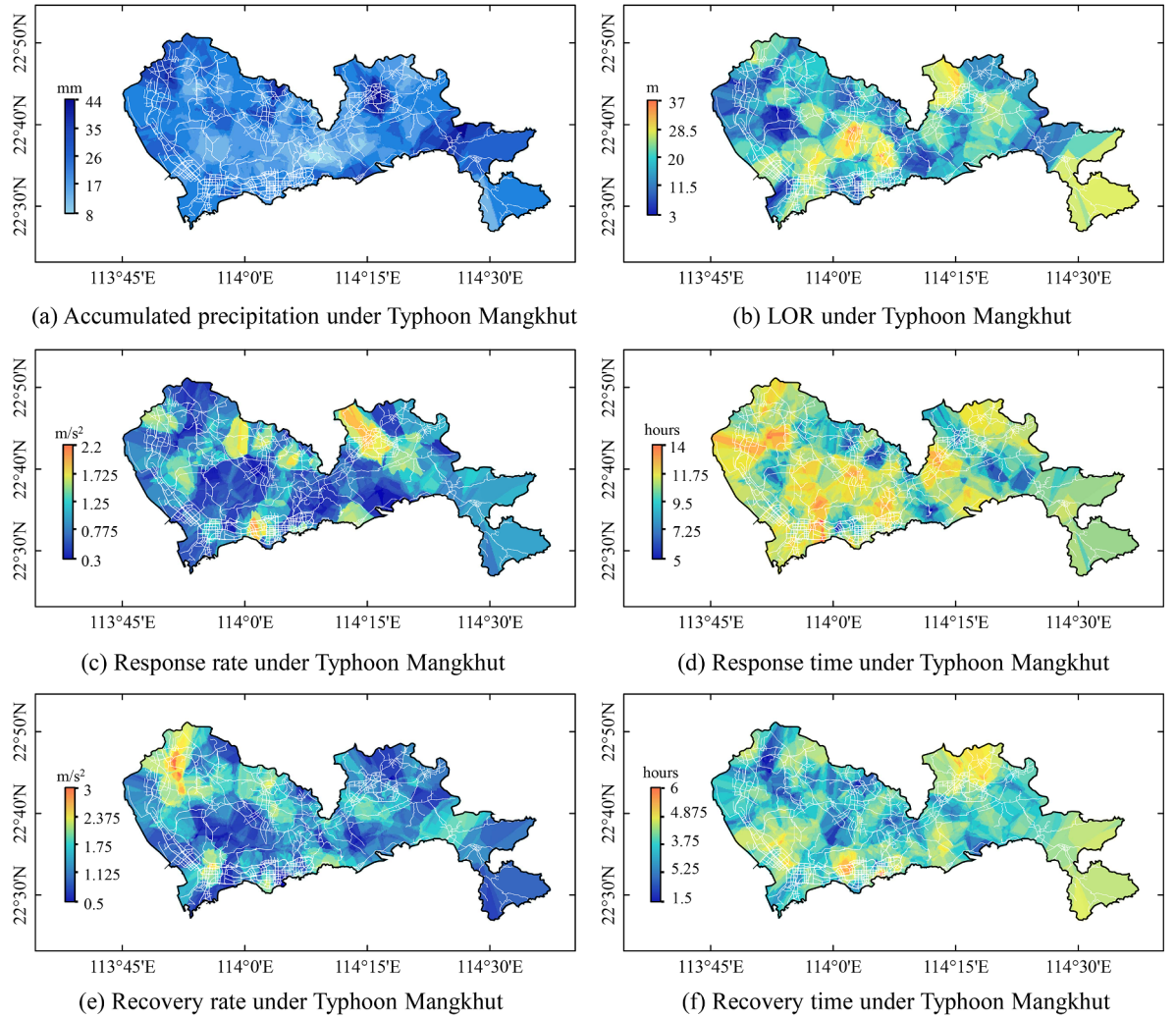


Fig. 11. Spatial characteristics of observed resilience in Shenzhen under Typhoon Mangkhut.

the accuracy of *LoR* predictions in highway (level 00) and expressway (level 01) is the highest among all roads, but keeps relatively stable when precipitation grows. However, there is a notable drop when precipitation exceeds 50 mm. All these results under Typhoon Mangkhut is generally consistent with the characteristics of resilience predictions in general precipitation events in Fig. 8(c) and (d). These results indicate that the proposed model can keep prediction errors around 7% for *LoR*, but lose some performance in the roads with severe local precipitation. The predictive errors of response rate are significantly lower than that of recovery rate in Fig. 8(g) and (h), and the precision gap between them is similar for most of levels of road as well as intensities of precipitation. Overall, *LoR* achieves the smallest prediction error among all groups, compared with the precision of response rate (about 11%) and recovery rate (about 13%). The above findings indicate that the total failure degree of transportation system is easy to be estimated accurately, but the exact processes of shutdown and restoration are hard to be forecasted.

The spatial characteristics of speed and resilience predictions under Typhoon Mangkhut are shown in Figs. 9(d)–(f) and 10(d)–(f). In the bay area of Shenzhen, the statistical indices of speed prediction are significantly higher than that of other areas, as shown in Fig. 9(d)–(f). This phenomenon is probably caused by the change of travel demand under the threat of coast flooding. In Fig. 10(d)–(f), the spatial distributions of relative errors of *LoR*, response rate, and recovery rate under Typhoon Mangkhut are almost inverse to the observed resilience spatial patterns in Fig. 11(b), (c) and (e). The results illustrate that the roads with less loss of observed resilience present higher precision of prediction. Overall, the spatial distributions of resilience prediction present strong local characteristics caused by the effects of Typhoon Mangkhut.

5. Conclusions

In this study, a novel end to end deep learning framework is proposed to estimate and predict the spatiotemporal patterns of transportation resilience under extreme weather events. The framework is based on the Diffusion Graph Convolutional Recurrent

Neural Network (DCRNN) and the dynamic-capturing algorithm of resilience. The model can fully extract and adaptively learn the spatiotemporal features of urban transportation network, with integrating temporal and topological-spatial modeling. The on-demand ride services data provided by DiDi Chuxing and auxiliary grid meteorological data are employed to estimate the characteristics of real-world transportation resilience and validate the spatiotemporal predictions of resilience. There are several contributions of this research: (1) This work is one of the few data-driven attempts modeling and predicting urban transportation resilience under extreme weather events; (2) The indices and methods evaluating resilience are designed specially to match the real data in the traffic monitoring network, which are further attempts to extend the existing methodology of resilience evaluation to broader real-world situations under disasters, and to more practical applications in emergency preparedness and response procedures; (3) The proposed framework is proven to have excellent performance on estimation and prediction of resilience and strong potential to be updated continuously with the development of spatiotemporal deep learning models, and could be widely-used in general resilience research except that in urban road network; (4) The proposed model is confirmed to strongly improve the ability of modeling the abnormal fluctuation of traffic conditions under extreme weather events, with adoption of DCRNN, directed graph, specialized feature engineering and external data input; (5) The proposed framework can evaluate and predict resilience based on plenty of extreme weather events instead of the case study focusing on a certain disaster event, which can derive more general conclusion; (6) The aggregate data of related precipitation events can be utilized to model transportation resilience under extreme weather events if there is sample imbalance problem due to limited historical disaster data. Several findings from this study are summarized as follows.

In terms of observed transportation resilience: (1) The degradation of system performance on urban road network and the time of adapting to the disruptions increase rapidly when the external disrupts upgrade, but the time of recovery process is not sensitive to levels of disasters; (2) The time of response process is double or triple of that of recovery process in both general precipitation and extreme weather events; (3) The scale of failure is larger, and speed of adapting to failures is lower on sparse urban transportation network; (4) An elastic limit probably exists in the recovery process of transportation resilience. In general precipitation events, the system demonstrates elasticity characteristics that serious impacts cause rapid restoration. In extreme weather events, the system presents plasticity characteristics that severe disruptions cause slow recovery.

In terms of resilience prediction: (1) The proposed model can effectively predict transportation resilience and outperform the competitors in terms of accuracy; (2) Compared with undirected graph, directed graph fits the model better in terms of improving prediction performance; (3) Meteorological features and historical speed data present different mechanisms in enhancing the model prediction performance, and integrating both external features can further improve the prediction precision; (4) Generally, the prediction accuracy of resilience indices decreases with the loss of resilience, response rate, and recovery rate. The total scales of failures are easy to be predicted, but exact processes of shutdown and restoration are hard to be forecasted.

The derived results and conclusions will have practical implications for the management of urban road network under extreme weather events. The real-world characteristics of transportation resilience can assist policy makers clearly understand the process of resilience variation and differences between general precipitation and catastrophic events. The proposed framework and spatiotemporal prediction results of resilience would help urban transport management departments prejudge the specific status and variation trends of urban traffic before and during disasters in advance, and build efficient emergency preparedness and response procedures.

A limitation of this paper is that the dataset only includes 21-month on-demand ride services data and is lack of observed traffic volume data. Longer time-span traffic data can include more precipitation events and thus derive more reliable results. Volume data can provide further information exploring reasons of resilience variation. In future studies, we expect to build a more efficient model to capture spatiotemporal dependency and handle more extreme weather events.

Declaration of Competing Interest

The authors declare that they have no known competing financial interests or personal relationships that could have appeared to influence the work reported in this paper.

Acknowledgements

This research is funded by the National Planning Office of Philosophy and Social Science (No. 16ZDA048), the National Natural Science Foundation of China (No. 71971029) and the Huo Yingdong Education Foundation (No. 171069). The authors also thank the DiDi Athena Joint Talent Program and the China Scholarship Council (No. 201506230117) for supporting this work. The comments of anonymous reviewers are acknowledged which contributed to important improvements of this paper.

Appendix A. Supplementary material

Part of the source code in this article is available at https://github.com/Charles117/resilience_shenzhen.

References

- Aksu, D.T., Ozdamar, L., 2014. A mathematical model for post-disaster road restoration: enabling accessibility and evacuation. *Transp. Res. Part E: Logistics Transp. Rev.* 61, 56–67.
 Atwood, J., Towsley, D., 2016. Diffusion-convolutional neural networks. *Adv. Neural Inform. Process. Syst.* 1993–2001.

- Bahdanau, D., Cho, K., Bengio, Y., 2014. Neural machine translation by jointly learning to align and translate. arXiv preprint arXiv:1409.0473.
- Bruna, J., Zaremba, W., Szlam, A., LeCun, Y., 2013. Spectral networks and locally connected networks on graphs. arXiv preprint arXiv:1312.6203.
- Bruneau, M., Chang, S.E., Eguchi, R.T., Lee, G.C., O'Rourke, T.D., Reinhorn, A.M., Shinozuka, M., Tierney, K., Wallace, W.A., Von Winterfeldt, D., 2003. A framework to quantitatively assess and enhance the seismic resilience of communities. *Earthquake Spectra* 19 (4), 733–752.
- Cats, O., Jenelius, E., 2015. Planning for the unexpected: the value of reserve capacity for public transport network robustness. *Transp. Res. Part A: Policy Practice* 81, 47–61.
- Chen, X.-Z., Lu, Q.-C., Peng, Z.-R., Ash, J.E., 2015. Analysis of transportation network vulnerability under flooding disasters. *Transp. Res. Rec.* 2532 (1), 37–44.
- Cho, K., Van Merriënboer, B., Gulcehre, C., Bahdanau, D., Bougares, F., Schwenk, H., Bengio, Y., 2014. Learning phrase representations using RNN encoder-decoder for statistical machine translation. arXiv preprint arXiv:1406.1078.
- Cui, Z., Henrickson, K., Ke, R., Wang, Y., 2019. Traffic graph convolutional recurrent neural network: a deep learning framework for network-scale traffic learning and forecasting. *IEEE Trans. Intell. Transp. Syst.*
- Defferrard, M., Bresson, X., Vandergheynst, P., 2016. Convolutional neural networks on graphs with fast localized spectral filtering. *Adv. Neural Inform. Process. Syst.* 3844–3852.
- Donovan, B., Work, D.B., 2017. Empirically quantifying city-scale transportation system resilience to extreme events. *Transp. Res. Part C: Emerg. Technol.* 79, 333–346.
- Fu, R., Zhang, Z., Li, L., 2016. Using LSTM and GRU neural network methods for traffic flow prediction. In: 2016 31st Youth Academic Annual Conference of Chinese Association of Automation (YAC). IEEE, pp. 324–328.
- Guo, S., Lin, Y., Li, S., Chen, Z., Wan, H., 2019. Deep spatial-temporal 3D convolutional neural networks for traffic data forecasting. *IEEE Trans. Intell. Transp. Syst.* 20 (10), 3913–3926.
- Hao, S., Lee, D.-H., Zhao, D., 2019. Sequence to sequence learning with attention mechanism for short-term passenger flow prediction in large-scale metro system. *Transp. Res. Part C: Emerg. Technol.* 107, 287–300.
- Hechtlinger, Y., Chakravarti, P., Qin, J., 2017. A generalization of convolutional neural networks to graph-structured data. arXiv preprint arXiv:1704.08165.
- Hochreiter, S., Schmidhuber, J., 1997. Long short-term memory. *Neural Comput.* 9 (8), 1735–1780.
- Huang, X., Sun, J., Sun, J., 2018. A car-following model considering asymmetric driving behavior based on long short-term memory neural networks. *Transp. Res. Part C: Emerg. Technol.* 95, 346–362.
- Jenelius, E., 2018. Public transport experienced service reliability: Integrating travel time and travel conditions. *Transp. Res. Part A: Policy Practice* 117, 275–291.
- Ke, J., Zheng, H., Yang, H., Chen, X.M., 2017. Short-term forecasting of passenger demand under on-demand ride services: a spatio-temporal deep learning approach. *Transp. Res. Part C: Emerg. Technol.* 85, 591–608.
- Kepaptsoglou, K.L., Konstantinou, M.A., Karlaftis, M.G., Stathopoulos, A., 2014. Planning postdisaster operations in a highway network: network design model with interdependences. *Transp. Res.* 459 (1), 1–10.
- Li, Y., Yu, R., Shahabi, C., Liu, Y., 2017. Diffusion convolutional recurrent neural network: Data-driven traffic forecasting. arXiv preprint arXiv:1707.01926.
- Liao, B., Zhang, J., Wu, C., McIlwraith, D., Chen, T., Yang, S., Guo, Y., Wu, F., 2018. Deep sequence learning with auxiliary information for traffic prediction. In: Proceedings of the 24th ACM SIGKDD International Conference on Knowledge Discovery & Data Mining, pp. 537–546.
- Lin, L., He, Z., Peeta, S., 2018a. Predicting station-level hourly demand in a large-scale bike-sharing network: a graph convolutional neural network approach. *Transp. Res. Part C: Emerg. Technol.* 97, 258–276.
- Lin, Y., Mago, N., Gao, Y., Li, Y., Chiang, Y.-Y., Shahabi, C., Ambite, J.L., 2018b. Exploiting spatiotemporal patterns for accurate air quality forecasting using deep learning. In: Proceedings of the 26th ACM SIGSPATIAL International Conference on Advances in Geographic Information Systems, pp. 359–368.
- Loo, B.P., Leung, K.Y., 2017. Transport resilience: the occupy central movement in Hong Kong from another perspective. *Transp. Res. Part A: Policy Practice* 106, 100–115.
- Lu, Q.-C., 2018. Modeling network resilience of rail transit under operational incidents. *Transp. Res. Part A: Policy Practice* 117, 227–237.
- Lu, Q.-C., Zhang, J., Peng, Z.-R., Rahman, A.S., 2014. Inter-city travel behaviour adaptation to extreme weather events. *J. Transp. Geogr.* 41, 148–153.
- Ma, X., Tao, Z., Wang, Y., Yu, H., Wang, Y., 2015. Long short-term memory neural network for traffic speed prediction using remote microwave sensor data. *Transp. Res. Part C: Emerg. Technol.* 54, 187–197.
- Ma, X., Zhang, J., Du, B., Ding, C., Sun, L., 2018. Parallel architecture of convolutional bi-directional lstm neural networks for network-wide metro ridership prediction. *IEEE Trans. Intell. Transp. Syst.* 20 (6), 2278–2288.
- Mattsson, L.-G., Jenelius, E., 2015. Vulnerability and resilience of transport systems—A discussion of recent research. *Transp. Res. Part A: Policy Practice* 81, 16–34.
- Schuster, M., Paliwal, K.K., 1997. Bidirectional recurrent neural networks. *IEEE Trans. Signal Process.* 45 (11), 2673–2681.
- Sun, L., Yin, Y., 2017. Discovering themes and trends in transportation research using topic modeling. *Transp. Res. Part C: Emerg. Technol.* 77, 49–66.
- Sutskever, I., Vinyals, O., Le, Q.V., 2014. Sequence to sequence learning with neural networks. *Adv. Neural Inform. Process. Syst.* 3104–3112.
- Testa, A.C., Furtado, M.N., Alipour, A., 2015. Resilience of coastal transportation networks faced with extreme climatic events. *Transp. Res. Rec.* 2532 (1), 29–36.
- Wang, Y., Skerry-Ryan, R., Stanton, D., Wu, Y., Weiss, R.J., Jaitly, N., Yang, Z., Xiao, Y., Chen, Z., Bengio, S., 2017. Tacotron: Towards end-to-end speech synthesis. arXiv preprint arXiv:1703.10135.
- Wang, H.W., Li, X.B., Wang, D., Zhao, J., He, H.D., Peng, Z.R., 2020. Regional prediction of ground-level ozone using a hybrid sequence-to-sequence deep learning approach. *J. Clean Prod.* 253, 119841. <https://doi.org/10.1016/j.jclepro.2019.119841>.
- Wu, Y., Tan, H., 2016. Short-term traffic flow forecasting with spatial-temporal correlation in a hybrid deep learning framework. arXiv preprint arXiv:1612.01022.
- Wu, Y., Tan, H., Qin, L., Ran, B., Jiang, Z., 2018. A hybrid deep learning based traffic flow prediction method and its understanding. *Transp. Res. Part C: Emerg. Technol.* 90, 166–180.
- Yang, S., Ma, W., Pi, X., Qian, S., 2019. A deep learning approach to real-time parking occupancy prediction in transportation networks incorporating multiple spatio-temporal data sources. *Transp. Res. Part C: Emerg. Technol.* 107, 248–265.
- Yu, B., Yin, H., Zhu, Z., 2017. Spatio-temporal graph convolutional networks: A deep learning framework for traffic forecasting. arXiv preprint arXiv:1709.04875.
- Zhang, Y., Cheng, T., Ren, Y., 2019a. A graph deep learning method for short-term traffic forecasting on large road networks. *Comput.-Aided Civ. Infrastruct. Eng.* 34 (10), 877–896.
- Zhang, Z., Li, M., Lin, X., Wang, Y., He, F., 2019b. Multistep speed prediction on traffic networks: a deep learning approach considering spatio-temporal dependencies. *Transp. Res. Part C: Emerg. Technol.* 105, 297–322.
- Zhu, Y., Xie, K., Ozbay, K., Zuo, F., Yang, H., 2017. Data-driven spatial modeling for quantifying networkwide resilience in the aftermath of hurricanes Irene and Sandy. *Transp. Res. Rec.* 2604 (1), 9–18.